We are IntechOpen,
the world's leading publisher of
Open Access books
Built by scientists, for scientists

6,900
Open access books available

186,000
International authors and editors

200M
Downloads

154
Countries delivered to

Our authors are among the

TOP 1%
most cited scientists

12.2%
Contributors from top 500 universities

CLARIVATE ANALYTICS
BOOK CITATION INDEX
INDEXED

WEB OF SCIENCE™

Selection of our books indexed in the Book Citation Index
in Web of Science™ Core Collection (BKCI)

Interested in publishing with us?
Contact book.department@intechopen.com

Numbers displayed above are based on latest data collected.
For more information visit www.intechopen.com

Stress Measurements in Si and SiGe by Liquid-Immersion Raman Spectroscopy

Daisuke Kosemura, Motohiro Tomita, Koji Usuda and Atsushi Ogura

Additional information is available at the end of the chapter

1. Introduction

Strained Si technology is important for engineering field-effect transistors (FETs) [1,2]. There are two types of the strained Si technologies. One is so-called global strained Si technology. Another is so-called local strained Si technology. The former is the technology of using a strained Si substrate which has a several-dozen-nanometers-thick strained Si layer at the top of the substrate [3-5]. The strained Si layer is obtained by growing Si on SiGe, therefore, large tensile strain with biaxial isotropy can be induced in Si. The isotropic biaxial tensile strain in Si allows for performance improvements for both of n- and p- type FETs. Homogeneous strain distribution can be obtained under the critical thickness of the strained Si layer [6].

In the latter case, the strain is induced only in the desired region, the channel region of FET [7,8]. A SiN film is used as the stressor that can induce tensile or compressive uniaxial stress in Si by changing the deposition conditions of the SiN film [9,10]. The uniaxial tensile strain enhances electron mobility, while the uniaxial compressive strain enhances hole mobility. Various kinds of the local strained Si techniques have so far been suggested by many researchers [11,12]. The combination of the global and local strained Si technologies is considered effective to induce extremely large strain in Si. Fin-type structures have been reported for high-performance FETs [13]. It is considered that the stress relaxation occurs during the fabrication of the fin-shaped strained Si layer. There are many other origins of strain fluctuations, e.g., shallow trench isolation (STI), metal gate electrodes, silicide, interconnections, and its layout. As a result, the stress states in the future generation FETs become complicated. The relationship between the electrical properties of FETs and the strain is also complicated. Therefore, to measure the complicated stress states in Si has great demand in order to improve the FET performance effectively.

Several kinds of strain or stress measurements have been studied, e.g., X-ray diffraction (XRD), transmission electron microscopy (TEM), electron backscattering diffraction (EBSD), and Raman spectroscopy [4,14-16]. Among them, Raman spectroscopy has the advantages such as high sensitive to local strain, submicron spatial resolution, nondestructive measurements, fast measurements, and ease of use. Consequently, Raman spectroscopy has been frequently used by many researchers to measure the strain in Si [3,7-9,17-21]. However, conventional Raman spectroscopy fails to measure the complicated stress states in Si. The reason is as follows. Backscattering geometry from a (001) Si substrate is generally used in Raman measurements of strained Si. In this geometry, only one of three optical phonon modes is Raman active, while two of three modes are Raman inactive. The limitation arises from the extremely high symmetry of the Si crystal. As a result, the weighted average value of the complicated stress state is obtained, that is, it is impossible to perform quantitative measurements of strain by conventional Raman spectroscopy.

Si has three optical phonon modes: one longitudinal optical (LO) phonon mode and two transverse optical (TO) phonon modes, the polarizations of which are parallel and perpendicular to the phonon wave vector, respectively. Recently, the forbidden optical phonon modes, the TO phonon modes, were excited even under the (001) Si backscattering geometry, using a high-numerical aperture (NA) liquid-immersion lens [22-24]. If all of the three optical phonon modes are detectable, the unknown three components of a stress tensor in Si can be obtained in theory [25-35]. The high-NA liquid-immersion Raman spectroscopy has great potential for measuring the complicated stress states in Si with high spatial resolution.

On the other hand, the number of stress tensor components is six. Therefore, the evaluation of nondiagonal stress components, shear stress components, is considered difficult even detecting the TO phonon modes. The shear stress is often generated at the discontinuous region, e.g., around STI and at the edge of a contact etch stop layer. The shear stress often produces dislocations in Si, which cause leakage current during transistor operation [36,37]. The shear stress measurements are desired for failure analysis. The induction of the stress with the nondiagonal components requires the transformation of the Raman tensors. Therefore, Raman spectroscopy is essentially sensitive to the shear stress.

In this study, anisotropic stress states in Si were measured by the high-NA liquid-immersion Raman spectroscopy. Strained SiGe was also measured by the same technique. SiGe has been suggested as the channel material of next generation FETs, because the both mobilities of electrons and holes in SiGe are higher than those in Si. Furthermore, the strain induction in SiGe is considered effective for improving electrical properties of SiGe FETs in the same way as strained Si [38-41]. The nondiagonal stress components, shear stress components, were measured by analyzing the dependence of Raman spectra on the relative polarization direction between sample orientation and electrical fields of incident and scattered light.

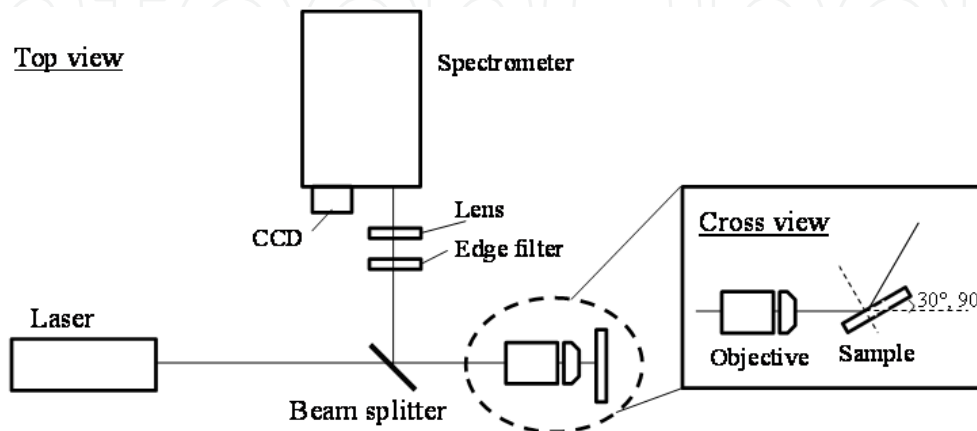## 2. Experimental procedure

2.1. Excitation of TO phonon modes

The Raman intensity is calculated by the following equation [42];

$$I \propto \sum_j \left| e_s{}^T R_j e_i \right|^2 , \tag{1}$$

$$R_1 = \begin{pmatrix} 0 & 0 & 0 \\ 0 & 0 & d \\ 0 & d & 0 \end{pmatrix}, R_2 = \begin{pmatrix} 0 & 0 & d \\ 0 & 0 & 0 \\ d & 0 & 0 \end{pmatrix}, R_3 = \begin{pmatrix} 0 & d & 0 \\ d & 0 & 0 \\ 0 & 0 & 0 \end{pmatrix}, \tag{2}$$

where R_j is the Raman tensors of Si [43]. e_i and e_s are the electrical fields of incident and scattered light, respectively. The superscript T denotes transpose. From Eqs. (1) and (2), the TO phonon modes are not excited under the (001) Si backscattering geometry. This is because the component of z polarization of the incident light is reduced to almost zero in the case of the (001) Si backscattering configuration. The z polarization is thus needed to excite the TO phonon modes in Si. It is considered that oblique light relative to the (001) Si surface gives rise to the z polarization.

Fig. 1 shows the experimental set-up for oblique incident light configuration in this study. The glancing angles of the laser against the sample were 30° and 90°, as shown in Fig. 1. Fig. 2 shows the examples of calculations for the Raman intensities in the 90° and 30° configurations, using Eqs. (1) and (2). In the case of the 90° configuration, the (001) Si backscattering configuration, the TO phonon modes are Raman inactive and the LO phonon mode is Raman active, as mentioned above. On the other hand, in the case of the 30° configuration, the oblique incident light configuration, the TO phonon mode is Raman active. This fact arises because the z polarization of the incident light can be obtained in the oblique incident light configuration. In the rough approximations, the Raman intensities are considered to be the same for the 90° and 30° configurations, as shown in Fig. 2.

Figure 1. Experimental set-up for oblique incident light configuration

Figure 2. Calculations of Raman intensities for 90° and 30° configurations.

The intensity ratio of the TO phonon mode to the LO phonon mode in the 30° configuration is calculated to be;

$$\frac{I_{TO}}{T_{LO}} = \frac{|d\sin\theta|^2}{|d\cos\theta|^2} \approx 0.046 \, , \tag{3}$$

where θ is the aperture angle in Si. In the 30° configuration, θ is approximately 12.13° in the case of λ = 532 nm laser because Si has the large refraction index [44]. Therefore, the intensity of the TO phonon mode are much small, compared to that of the LO phonon mode even in the 30° configuration. The detection of the TO phonon modes is basically considered difficult. Moreover, for the oblique incident light configuration, high-resolution measurements cannot be achieved because it is difficult to use the high-NA lens and the beam spot becomes an ellipse. In this study, the high-NA liquid-immersion lens was used in order to obtain the oblique light relative to the (001) Si surface.

An aperture angle θ is calculated by NA = $n \times \sin\theta$ (where n is a refractive index). θ is equal to 44.4° in conventional Raman spectroscopy with the use of NA = 0.7 objective (n = 1.0). On the other hand, θ is equal to 69.0° in high-NA liquid-immersio Raman spectroscopy with the NA = 1.4 liquid-immersio lens (n = 1.5). However, the incident light widely refracts at the interface of the Si surface because Si has the large refractive index as mentioned above. The refractive index of Si for the λ = 364 nm light (where λ is wavelength) is approximately 6.5 [44]. Therefore, θ in Si results in 6.2° in conventional Raman spectroscopy (NA = 0.7). This configuration is almost under the (001) Si backscattering geometry, i.e., the component of the z polarization is reduced to almost zero. This fact causes that the TO phonon modes are Raman inactive in conventional Raman spectroscopy. On the other hand, θ in Si results in 12.4° in high-NA liquid-immersio Raman spectroscopy (NA = 1.4). It is considered that the value of θ in Si is still small to excite the TO phonon modes effectively, although the value is

two times larger than that in conventional Raman spectroscopy. It is considered that the use of the UV light has the drawback for the excitation of the TO phonon modes. In the case of visible light (λ = 532 nm), θ in Si are calculated to be 9.8° and 19.8° in conventional and liquid-immersion Raman spectroscopy, respectively. The value for oil-immersion Raman spectroscopy with the use of the visible light is relatively large, therefore, the large component of the z polarization is obtained. Table 1 shows θs as a function of NA. θ_1 and θ_2 are the aperture angles in the medium and Si, respectively.

NA	With use of UV light (λ = 364 nm)			With use of visible light (λ = 532 nm)		
	θ_1	θ_2	TO/LO	θ_1	θ_2	TO/LO
0.7	44.4	6.2	0.06	44.4	9.8	0.25
1.1	57.8	9.7	0.2	57.8	15.5	1.0
1.2	67.4	10.6	0.3	67.4	16.9	1.3
1.4	69.0	12.4	0.5	69.0	19.8	2.0
1.7	-----	-----	-----	70.8	24.4	3.8

Table 1. θs with use of visible and UV light and intensity ratio of TO to LO phonon modes as a function of NA.

It is important to choose the appropriate NA and the wavelength for the excitation of the TO phonon modes. The intensity of the TO phonon mode excited by high-NA liquid-immersion Raman spectroscopy is estimated as follows. The TO phonon modes are excited mainly by the marginal ray of incident light. The Raman intensity can be calculated by the following equation [45]:

$$S_\Omega = A\sum_j \int_{\Omega_s} \int_{\Omega_i} \left(e_i R_j e_s\right)^2 d\Omega_i d\Omega_s , \qquad (4)$$

where Ω_i and Ω_s are the solid angles of incident and scattered light, respectively. The intensity ratio of the TO to LO phonon modes is considered to be the intensity ratio of the z component of the marginal ray to the paraxial ray. Fig. 3 shows the intensity ratio of TO to LO phonon modes as a function of NA with the use of visible light. The aperture angle dependence on NA is also shown in Fig. 3.
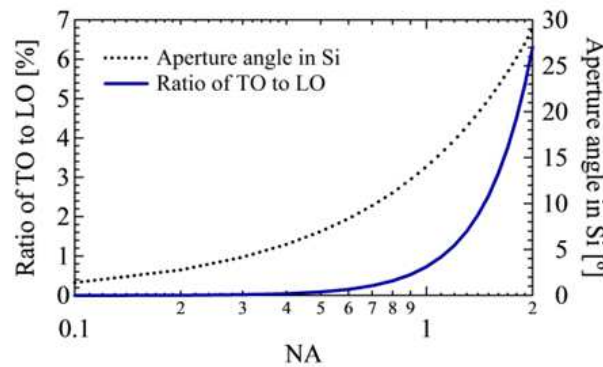
Figure 3. Intensity ratio of TO to LO phonon modes and aperture angle in Si vs. NA
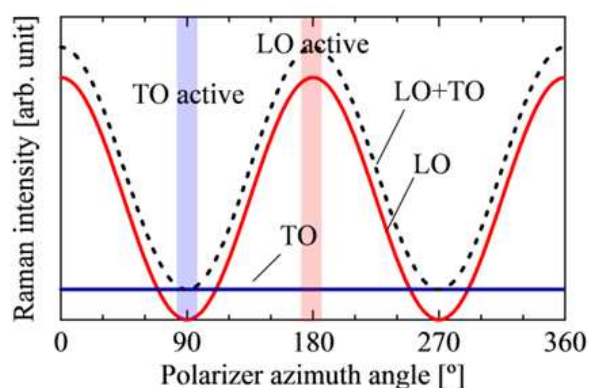
Figure 4. Raman intensities of LO and TO phonon modes vs polarizer azimuth angle

The intensity ratio of the TO to LO phonon modes as well as the aperture angle in Si increases with the increase in NA. Note that drastic increase is confirmed especially beyond NA = 1.0 for the intensity ratio of TO to LO. The value is approximately 2.0% for NA = 1.4 with the use of visible light, while the value is approximately 0.5% with the use of UV light, as shown in Table 1. From the estimations, the intensity of the TO phonon mode is very low, compared to that of the LO phonon mode. Actually, it is important to suppress the intensity of the LO phonon mode for the excitation of the TO phonon modes. This can be accomplished by the Raman polarization selection rules [42].

Fig. 4 shows the Si Raman intensities of the LO and TO phonon modes calculated by Eq. (1) as a function of a polarizer azimuth angle. For the LO phonon mode, the intensity changes in the period of 180°. On the other hand, for the TO phonon mode, the intensity is independent on the polarizer azimuth angle (the value is exaggerated for ease to view). This is because the component of the z polarization obtained by the oblique light remains constant all over the angles. As a result, the measurable Raman intensity profile is the sum of the intensities of the LO and TO phonon modes, which is shown by the dashed line in Fig. 4. From Fig. 4, the LO phonon mode can be detected at the polarizer azimuth angle of 0°, 180°, and 360°. These correspond to the LO active configurations. On the other hand, the TO phonon mode can be detected at the angle of 90° and 270°. These correspond to the TO active configurations. The TO and LO phonon modes can be separately detected by the Raman polarization selection rules. It is possible to evaluate complicated stress states in Si by analyzing multi-optical phonon modes.

2.2. Methodology of measurements for anisotropic biaxial stress states in Si

In this section, the methodology of measurements for anisotropic biaxial stress states in Si by liquid-immersion Raman spectroscopy is shown. In the previous section, it was shown that the z polarization can be created by the oblique light due to the high-NA liquid-immersion lens. Consequently, the TO phonon modes in Si can be excited by the z polarization even under the (001) Si backscattering geometry. The TO phonon modes allow for the measurements of the anisotropic biaxial stress states in Si.

The force constant of a Si crystal changes by the induction of strain. Consequently, the optical-phonon frequencies also change. The difference of the force constant ΔK is represented as a second-rank tensor. The eigenvalues of ΔK after the induction of the strain can be obtained by solving the secular equation [29]. The square roots of the eigenvalues correspond to the changes of the optical-phonon frequencies (the Raman wavenumber shifts). Three equations between the strain (stress) and the Raman wavenumber shifts are obtained because Si has three optical-phonon modes (two TOs and one LO).

Suppose that there is a linear relationship between ΔK and strain [26]. In a coordinate system of x: [100], y: [010], and z: [001], ΔK is represented as the following equation:

$$\Delta K = A\varepsilon , \tag{5}$$

$$A = \begin{pmatrix} p & q & q & 0 & 0 & 0 \\ q & p & q & 0 & 0 & 0 \\ q & q & p & 0 & 0 & 0 \\ 0 & 0 & 0 & 2r & 0 & 0 \\ 0 & 0 & 0 & 0 & 2r & 0 \\ 0 & 0 & 0 & 0 & 0 & 2r \end{pmatrix} , \tag{6}$$

where ε is a strain tensor. A is a fourth-rank tensor whose components are p, q, and r called phonon deformation potentials (PDPs). Generally, transistors are fabricated on (001) Si substrate in the direction of [110] Si. Therefore, the coordinate transformation makes analysis easy [46]. Second-rank and fourth-rank tensors are transformed in the coordinate system of x' = [110], y' = [−110], and z' = [001] by the following equations:

$$T_{ij} = a_{ik}a_{jl}T_{kl} , \tag{7}$$

$$T_{ijkl} = a_{im}a_{jn}a_{ko}a_{lp}T_{mnop} , \tag{8}$$

$$a = \begin{pmatrix} 1/\sqrt{2} & 1/\sqrt{2} & 0 \\ -1/\sqrt{2} & 1/\sqrt{2} & 0 \\ 0 & 0 & 1 \end{pmatrix} , \tag{9}$$

where T and a are a second- or fourth- rank tensor and a transformation matrix, respectively. Hence, Eq. (5) results in:

$$\Delta K' = A'\varepsilon' , \tag{10}$$

where the primes denote the components in the coordinate $x'y'z'$. The secular equation of $\Delta K'$ is below:

$$\begin{vmatrix} \Delta K_{xx}' - \lambda & \Delta K_{xy}' & \Delta K_{xz}' \\ \Delta K_{xy}' & \Delta K_{yy}' - \lambda & \Delta K_{yz}' \\ \Delta K_{xz}' & \Delta K_{yz}' & \Delta K_{zz}' - \lambda \end{vmatrix} = 0 , \tag{11}$$

where λ is the eigenvalues. An anisotropic biaxial stress state is represented as the following second-rank tensor:

$$\sigma' = \begin{pmatrix} \sigma_{xx}' & 0 & 0 \\ 0 & \sigma_{yy}' & 0 \\ 0 & 0 & 0 \end{pmatrix}, \tag{12}$$

where σ_{xx}' and σ_{yy}' are the stress components in the directions of [110] and [–110], respectively. Generally, stress induction changes not only optical-phonon frequencies but also Raman tensors. However, in the case of the stress tensors only with the diagonal components, there are no changes of the Raman tensors. Therefore, the Raman polarization selection rules after the induction of the biaxial stresses σ_{xx} and σ_{yy} remains as those of stress-free Si [46]. The Raman tensors in the coordinate $x'y'z'$ are as follows [46]:

$$R_1' = \frac{1}{\sqrt{2}} \begin{pmatrix} 0 & 0 & d \\ 0 & 0 & d \\ d & d & 0 \end{pmatrix}, \ R_2' = \frac{1}{\sqrt{2}} \begin{pmatrix} 0 & 0 & d \\ 0 & 0 & -d \\ d & -d & 0 \end{pmatrix}, \ R_3' = \begin{pmatrix} d & 0 & 0 \\ 0 & -d & 0 \\ 0 & 0 & 0 \end{pmatrix} \tag{13}$$

Stress tensors are transformed to strain tensors by Hooke's law:

$$\varepsilon' = S'\sigma', \tag{14}$$

$$S = \begin{pmatrix} S_{11} & S_{12} & S_{12} & 0 & 0 & 0 \\ S_{12} & S_{11} & S_{12} & 0 & 0 & 0 \\ S_{12} & S_{12} & S_{11} & 0 & 0 & 0 \\ 0 & 0 & 0 & S_{44}/4 & 0 & 0 \\ 0 & 0 & 0 & 0 & S_{44}/4 & 0 \\ 0 & 0 & 0 & 0 & 0 & S_{44}/4 \end{pmatrix}, \tag{15}$$

where S expressed by Eq. (15) is the elastic compliance tensor. The components of S, S_{11}, S_{12}, and S_{44} are 7.68×10^{-12}, -2.14×10^{-12}, and 12.7×10^{-12} 1/Pa, respectively [17]. The transformation of the fourth-rank tensor S by Eq. (8) is needed. The strain tensor ε' expressed by Eq. (14) is substituted for Eq. (11) and then the eigenvalues λ_i are calculated. As a result, using Eq. (16), the relationship between the Raman wavenumber shifts $\Delta \omega$s and the anisotropic biaxial stresses σ_{xx}' and σ_{yy}' are obtained as follows [35]:

$$\lambda_i = \omega_i^2 - \omega_0^2 = (\omega_i + \omega_0)(\omega_i - \omega_0) \approx 2\omega_0(\omega_i - \omega_0), \ \Delta \omega_i \approx \frac{\lambda_i}{2\omega_0} . \tag{16}$$

$$\Delta\omega_1 = \frac{\lambda_1}{2\omega_0} = \frac{1}{2\omega_0}\left[\frac{1}{2}p(S_{11}+S_{12})+\frac{1}{2}q(S_{11}+3S_{12})+\frac{1}{2}rS_{44}\right]\times\sigma_{xx}'$$
$$+\frac{1}{2\omega_0}\left[\frac{1}{2}p(S_{11}+S_{12})+\frac{1}{2}q(S_{11}+3S_{12})-\frac{1}{2}rS_{44}\right]\times\sigma_{yy}' \tag{17-1}$$

$$\Delta\omega_2 = \frac{\lambda_2}{2\omega_0} = \frac{1}{2\omega_0}\left[\frac{1}{2}p(S_{11}+S_{12})+\frac{1}{2}q(S_{11}+3S_{12})-\frac{1}{2}rS_{44}\right]\times\sigma_{xx}'$$
$$+\frac{1}{2\omega_0}\left[\frac{1}{2}p(S_{11}+S_{12})+\frac{1}{2}q(S_{11}+3S_{12})+\frac{1}{2}rS_{44}\right]\times\sigma_{yy}' \tag{17-2}$$

$$\Delta\omega_3 = \frac{\lambda_3}{2\omega_0} = \frac{1}{2\omega_0}\left[pS_{12}+q(S_{11+}S_{12})\right]\times\left(\sigma_{xx}'+\sigma_{yy}'\right), \tag{17-3}$$

$$\Delta\omega_3 = \frac{\lambda_3}{2\omega_0} = \frac{1}{\omega_0}\left[\frac{S_{12}}{S_{11}+S_{12}}p+q\right]\times\varepsilon_{biaxial}=b\times\varepsilon_{biaxial}, \tag{18}$$

where b is so-called the b coefficient which is used for the evaluation of isotropic biaxial strain $\varepsilon_{biaxial}$ in strained Si substrates using the Raman wavenumber shift of the LO phonon mode $\Delta\omega_3$ [21,47].

Authors (year)	Sample	p/ω^2, q/ω^2, r/ω^2	b cm^{-1}	Citation
Anastassakis *et al.* (1970)[a]	Si bar	−1.25, −1.87, −0.66	−721	4 (9%)
Chandrasekhar *et al.* (1978)[b]	Si bar	−1.43, −1.89, −0.59	−696	18 (40%)
Anastassakis *et al.* (1990)[c]	Si bar	−1.85, −2.31, −0.71	−830	15 (33%)
Nakashima *et al.* (2006)[d]	Strained Si substrate	----------	−723	1 (2%)
JEITA (2007)[e]	Strained Si substrate	----------	−769	1 (2%)
Others[f-j]	Strained Si substrate	----------	−1040 ~ −715	6 (13%)

[a]Reference 14, [b]Reference 15, [c]Reference 16, [d]Reference 12, [e]Reference 39, [f-j]Reference 46, 47, 71, 78, and 79.

Table 2. Various PDPs suggested so far and statistics of citations.

Various PDPs have so far been suggested by many researchers. The suggested PDPs and the citation count are shown in Table 2. Forty-five papers were confirmed. As shown in Table 2, the values of PDPs are fluctuated. Thirty-seven of forty-five papers, approximately eighty-two percent papers, referred PDPs suggested by the Cardona's group in 1970-1990. Nakashima *et al.* examined the b coefficient in detail using strained Si substrates by Raman spectroscopy and high-resolution XRD in 2006 [21]. Furthermore, the detailed investigation of the b coefficient was performed in the working group of Japan electronics and information technology industries association (JEITA) in 2007 [48]. Eight organizations attended the working group: three companies for XRD measurements, three companies and

one University for Raman measurements, and one company for Rutherford back scattering (RBS) measurements. The b coefficient of -769 cm^{-1} was obtained [16]. Extreme care is needed to choose appropriate PDPs.

In this study, the validity of three sets of PDPs was evaluated by liquid-immersion Raman spectroscopy: first, $p/\omega^2 = -1.25$, $q/\omega^2 = -1.87$, and $r/\omega^2 = -0.66$ reported by Anastassakis *et al.* in 1970 [49], second, $p/\omega^2 = -1.43$, $q/\omega^2 = -1.89$, and $r/\omega^2 = -0.59$ reported by Chandrasekhar *et al.* in 1978 [50], and third, $p/\omega^2 = -1.85$, $q/\omega^2 = -2.31$, and $r/\omega^2 = -0.71$ reported by Anastassakis *et al.* 1990 [51]. The first set of PDPs was obtained from the first investigation. The second set appears to be the most commonly used, and the third set is the most recently reported among the three sets of PDPs.

The relationship between Raman wavenumber shifts $\Delta\omega$s and the anisotropic biaxial stresses σ_{xx}' and σ_{yy}' are obtained by substituting PDPs shown above for Eq. (17). When PDPs reported by Anastassakis *et al.* in 1970 are used,

$$\Delta\omega_1 = -2.30 \times \sigma_{xx}' - 0.12 \times \sigma_{yy}',$$ (19-1)

$$\Delta\omega_2 = -0.12 \times \sigma_{xx}' - 2.30 \times \sigma_{yy}',$$ (19-2)

$$\Delta\omega_3 = -2.00 \times \sigma_{xx}' - 2.00 \times \sigma_{yy}'.$$ (19-3)

When PDPs reported by Chandrasekhar *et al.* in 1978 are used,

$$\Delta\omega_1 = -2.31 \times \sigma_{xx}' - 0.37 \times \sigma_{yy}',$$ (20-1)

$$\Delta\omega_2 = -0.37 \times \sigma_{xx}' - 2.31 \times \sigma_{yy}',$$ (20-2)

$$\Delta\omega_3 = -1.93 \times \sigma_{xx}' - 1.93 \times \sigma_{yy}'.$$ (20-3)

When PDPs reported by Anastassakis *et al.* in 1990 are used,

$$\Delta\omega_1 = -2.88 \times \sigma_{xx}' - 0.54 \times \sigma_{yy}',$$ (21-1)

$$\Delta\omega_2 = -0.54 \times \sigma_{xx}' - 2.88 \times \sigma_{yy}',$$ (21-2)

$$\Delta\omega_3 = -2.30 \times \sigma_{xx}' - 2.30 \times \sigma_{yy}'.$$ (21-3)

2.3. Methodology of measurements for nondiagonal stress components

In the case of the induction of stress with the only diagonal stress components, strain-modified phonon eigenvectors ξ_i's which are obtained by solving the secular equation expressed by Eq. (11) coincide with the coordinate $x'y'z'$. In this case, the Raman tensors of Si

remains in the same form expressed by Eq. (13). On the other hand, shear stress causes a deviation between the phonon wave vector and ξ_i's, i.e., in the case of the induction of stress with the nondiagonal stress components, ξ_i's no longer coincide with the coordinate $x'y'z'$ [52]. The difference between ξ_i' and the coordinate $x'y'z'$ requires a change of the Raman tensors. The new Raman tensors $R_i'^*$ is expressed by:

$$R_i'^* = \left(\xi_i'^* \cdot \xi_1' \right) R_1' + \left(\xi_i'^* \cdot \xi_2' \right) R_2' + \left(\xi_i'^* \cdot \xi_3' \right) R_3' , \qquad (22)$$

where $\xi_i'^*$ and ξ_i' are the strain-modified eigenvectors for the introduction of stress with the nondiagonal and only diagonal stress components, respectively. Assuming the stress tensor shown by Eq. (12), the Raman tensors R_i' changes to $R_i'^*$:

$$R_1'^* = \begin{pmatrix} \times & 0 & \times \\ 0 & \times & \times \\ \times & \times & 0 \end{pmatrix}, \; R_2'^* = \begin{pmatrix} 0 & 0 & \times \\ 0 & 0 & \times \\ \times & \times & 0 \end{pmatrix}, \; R_3'^* = \begin{pmatrix} \times & 0 & \times \\ 0 & \times & \times \\ \times & \times & 0 \end{pmatrix}, \qquad \text{(23-1)-(23-3)}$$

where $\times$ indicates nonzero components (each value is not always the same), some of which depend on the eigenvalues obtained by solving the secular equation of Eq. (11). $R_2'^*$ has the same form as the Raman tensor R_2' because of $\tau_{xy} = \tau_{yz} = 0$. Therefore, R_2' corresponds to the TO phonon mode with the eigenvector in the y' direction. On the other hand, $R_1'^*$ and $R_3'^*$ no longer correspond to purely transverse and longitudinal modes, respectively, because their eigenvectors do not coincide with the x' and z' axes, respectively. Consequently, the Raman intensity is changed by the nondiagonal stress components obeying the Raman polarization selection rules. The nondiagonal stress components can be evaluated by analyzing the dependence of the Raman spectra on the relative polarization direction between the sample orientation and the electrical fields of incident and scattered light. The methodology is described as follows.

The methodology for evaluating complicated stress states was reported by Ossikovski et al [33]. They employed an experimental configuration that used oblique incident light to observe the forbidden modes, i.e., the TO phonon modes. In our experiments, the high-NA liquid-immersion lens was used to observe the TO phonon modes. High spatial resolution was preserved in liquid-immersion Raman spectroscopy.

First, a stress tensor is considered, and then the strain tensor is calculated by Hooke's law by Eq. (14). The strain tensor is substituted for the secular equation of Eq. (11). Three phonon eigenfrequencies of Si have been determined so far. Si is a nonpolar cubic crystal, that is, there is no difference between the TO phonon modes and LO phonon mode [52]. As a result, the three determined phonon eigenfrequencies are independent of the phonon wave vector. Second, the Raman tensors are determined using Eq. (22). Their forms change when the nondiagonal stress components are nonzero. Subsequently, the Raman intensity of each phonon mode is calculated by the Raman polarization selection rules given by Eq. (1). Third, each Raman spectrum is considered to be a Lorentzian function $\Lambda_i(\omega)$ [35]:

$$\Lambda_i(\omega) = \frac{I_i \Gamma^2}{(\omega - \Omega_i)^2 + \Gamma^2}, \tag{24}$$

where ω, Ω_i, and Γ are the Raman shift, the phonon eigenfrequencies , and the half width at half maximum of the spectrum, respectively. It is considered difficult to analyze each spectrum of the TO and LO phonon modes. Therefore the effective phonon eigenfrequency Ω_{eff} is used as a representative value. The effective value is the weighted average of the phonon eigenfrequencies relative to their intensities, as expressed by the following equation [26]:

$$\Omega_{eff} = \sum_i \frac{I_i \Omega_i}{I_T}, \tag{25}$$

where I_T is the total intensity of the three phonon modes. Eq. (25) is valid because the strain-induced splitting between the TO and LO phonon modes is small, compared to Γ. An example of a spectrum with the effective phonon eigenfrequency and the spectra of the TO and LO phonon modes are shown in Fig. 5. A uniaxial stress σ_{xx}' of 1.0 GPa is assumed in the calculation. In Fig. 5, the Raman spectra with the eigenfrequencies of Ω_1, Ω_2, and Ω_3 appear, which correspond to the optical phonon modes with the eigenvectors x', y', and z', respectively. The dashed line shows the Raman spectrum with the weighted average eigenfrequency. The Raman signal of the TO phonon modes with the eigenvectors x' and y' are obtained by the z polarization due to the high-NA lens (the component of z polarization is enlarged for ease to view).
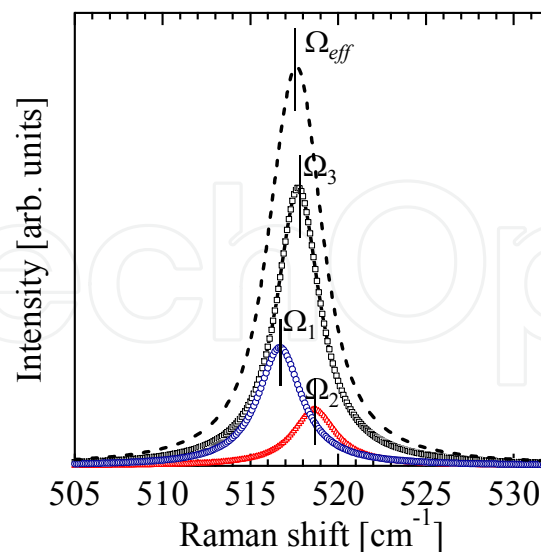
Figure 5. Raman spectrum with effective phonon frwuency and raman spectra with Ω_1, Ω_2, and Ω_3

Finally, the dependence of the Raman spectra on the polarization direction between the sample orientation and the electrical fields of incident and scattered light is obtained as

follows. The electrical fields of incident and scattered light are fixed in the y' direction. Regarding e_i, because the high-NA liquid-immersion lens is used, the z polarization can be obtained:

$$e_i = \frac{1}{\sqrt{1+\alpha^2}}\begin{pmatrix} 0 \\ 1 \\ \alpha \end{pmatrix}, \tag{26}$$

where α is the component of the z polarization. For $\alpha = 0$, this is correct in the (001) Si backscattering geometry. α was experimentally determined. Eq. (1) shows that for the Raman intensity, the rotations of the polarization directions of incident and scattered light are equivalent to the rotation of the sample, although the period for the sample rotation is half compared to those for the polarization rotations. In the experiments, the sample was rotated from 0° to 180°, which is represented by the following equations:

$$R_i'^*{}_{rot} = T R_i'^* T, \tag{27}$$

$$T(\phi) = \begin{pmatrix} \cos\varphi & \sin\varphi & 0 \\ -\sin\varphi & \cos\varphi & 0 \\ 0 & 0 & 1 \end{pmatrix}, \tag{28}$$

where $R_i'^*{}_{rot}$ and T are the Raman tensors after rotation by φ and the transformation matrix, respectively.

Fig. 6 shows the dependence of the effective Raman shifts on the sample rotation angle for the various stress states including hydrostatic stress, uniaxial stress, biaxial stress, and stress with the nondiagonal components, which are represented by:

$$\sigma_{hydrostatic} = \begin{pmatrix} 0.33 & 0 & 0 \\ 0 & 0.33 & 0 \\ 0 & 0 & 0.33 \end{pmatrix}, \quad \sigma_{uniaxial} = \begin{pmatrix} 1.0 & 0 & 0 \\ 0 & 0 & 0 \\ 0 & 0 & 0 \end{pmatrix}, \tag{29 and 30}$$

$$\sigma_{biaxial} = \begin{pmatrix} 0.5 & 0 & 0 \\ 0 & 0 & 0 \\ 0 & 0 & 0.5 \end{pmatrix}, \quad \sigma_{shear} = \begin{pmatrix} 0.5 & 0 & 0.5 \\ 0 & 0 & 0 \\ 0.5 & 0 & 0.5 \end{pmatrix}. \tag{31 and 32}$$

The above stress states correspond to the load of 1.0 GPa. A unique profile can be obtained for each stress state, as shown in Fig. 6. The profile for the hydrostatic stress remains constant all over the sample rotation angles because the degeneracy of the long-wavelength optical phonons does not lift under the hydrostatic stress. It should be noted that the profile becomes asymmetric only for the stress state with the nondiagonal components. As a result, the shear stress in Si is considered to be detectable by analyzing the dependence of the effective Raman shifts on the sample rotation angle.
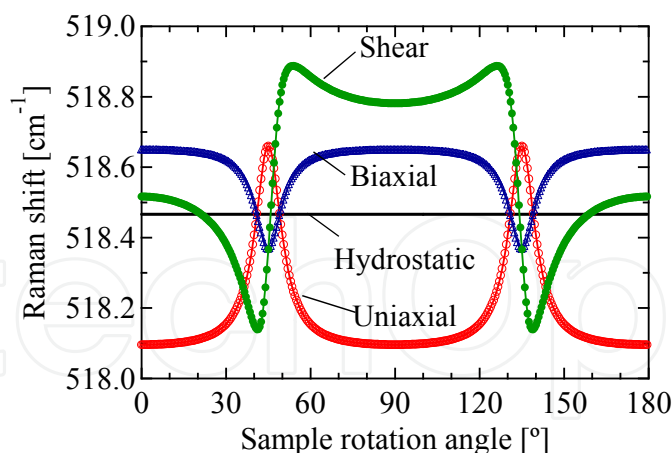
Figure 6. Effective Raman shift dependence on sample rotation angle for hydrostatic, uniaxial, biaxial, and shear stress.

2.4. Samples

(001)-oriented SSOI substrates were used as the samples [53,54]. Fig. 7(a) shows the cross sectional TEM image of the SSOI substrate. The structure of SSOI was strained Si layer/buried oxide (BOX) layer/Si substrate, which is the simplest structure among the strained Si substrates. The low-power consumption operation can be achieved due to the structure of Si on insulator (SOI) [55,56]. The thicknesses of the strained Si layers were 30, 50, and 70 nm. An isotropic biaxial tensile stress state exists in the strained Si layer.
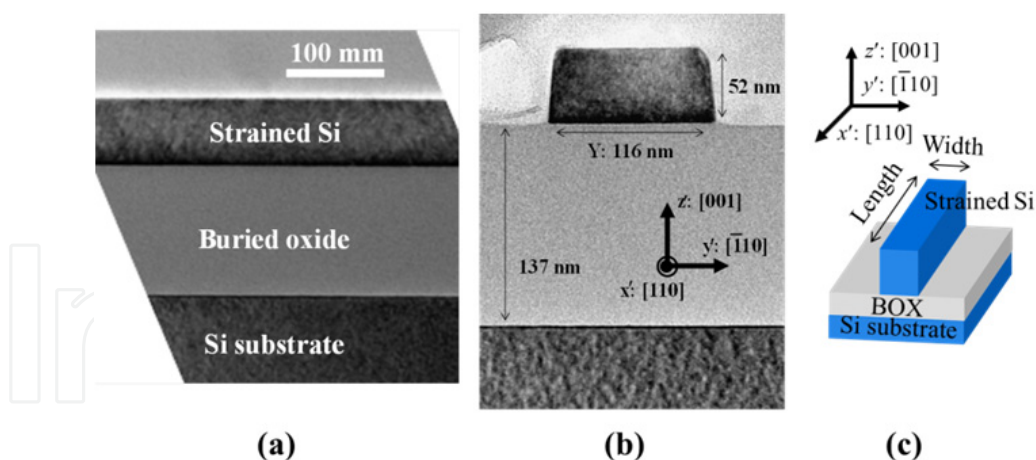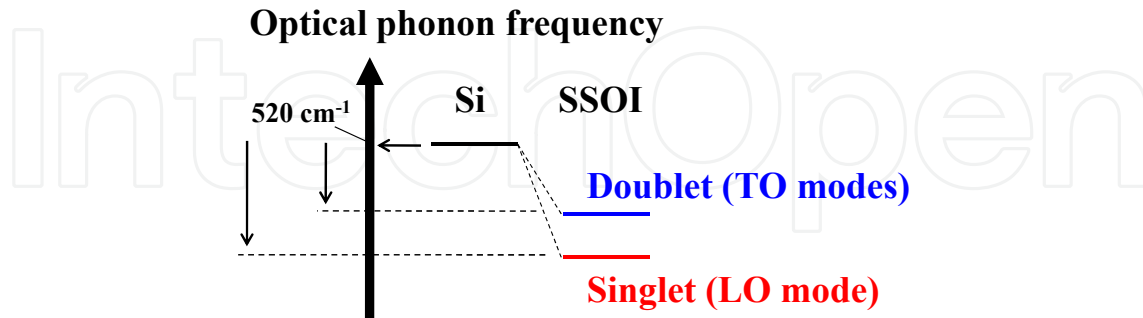

Figure 7. (a) Cross sectional TEM image of SSOI, (b) cross sectional TEM image of SSOI nanostructure, and (c) schematic of SSOI nanostructure

For Si, three long-wavelength optical phonon modes are degenerate at the center of the Brillouin zone. On the other hand, the degeneracy lifts after the induction of stress and the frequency of each mode individually shifts depending on the stress. For the isotropic biaxial tensile stress, the frequency of each mode shifts on the lower-frequency side and splits into singlet and doublet. In the case of (001) Si backscattering geometry, the singlet and doublet

correspond to the LO and TO phonon modes, respectively. Fig. 8 shows the optical phonon frequencies for Si and SSOI. Generally, the LO phonon mode which is Raman active under the (001) Si backscattering geometry is measured and the isotropic biaxial stress in the strained Si layer is evaluated using the b coefficient shown in Table 2.

Optical phonon frequency

Figure 8. Optical phonon frequencies for Si and SSOI

SSOI nanostructures were fabricated with arbitrary forms by electron beam (EB) lithography and reactive ion etching (RIE). Fig. 7(b) and (c) show the cross sectional TEM image and the schematic of the SSOI nanostructure. The coordinate system in the experiments is also shown in Fig. 7(b) and (c). The SSOI lengths (Ls) were 5.0, 3.0, 2.0, 1.5, 1.0, 0.8, and 0.5 μm. The SSOI widths (Ws) were 1.0, 0.5, 0.2, 0.1, and 0.05 μm. The SSOI nanostructure shapes were anisotropic. Therefore, the stress states are also considered anisotropic. The stress component in the z direction is considered to be zero because of free-standing surface. As a result, the stress tensors in the SSOI nanostructures are considered to be expressed by Eq. (12).

SiGe nanostructures were fabricated as the same manner. SiGe with approximately 30% Ge concentration was epitaxially grown on a Si substrate. The thickness of the SiGe layer was approximately 35 nm. The Ls and Ws of the SiGe nanostructures were the same as those of the SSOI nanostructures. The cross sectional TEM image and the schematic of the SiGe nanostructure are shown in Fig. 9(a) and (b), respectively. As shown in the TEM image, overetching of the Si substrate is confirmed.
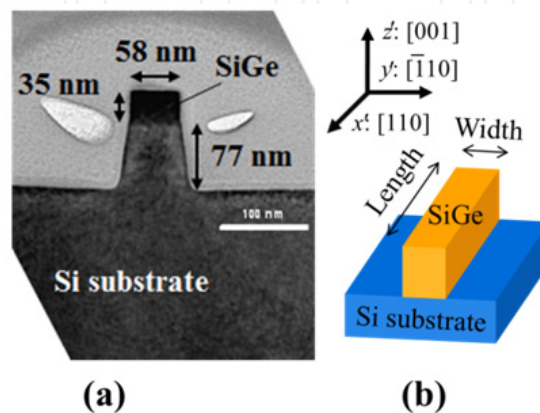
Figure 9. (a) Cross sectional TEM image of SiGe nanostructure and (b) schematic
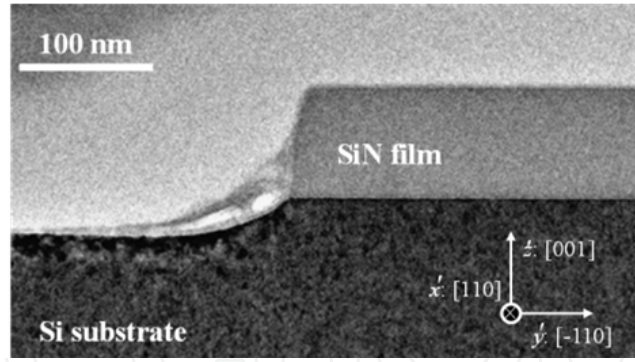
Figure 10. 10 TEM image of SiN film on Si substrate

A 80-nm-thick SiN film was deposited on a Si substrate by low-pressure vapor deposition. The inner stress of the SiN film was compressive due to its high density [10]. The compressive stress of approximately −1.0 GPa was observed by wafer bowing measurements [57]. Subsequently, the SiN film was etched to form an edge structure by EB and RIE. The cross-sectional TEM image of the sample is shown in Fig. 10. The stress distribution in Si around the SiN film edge was reproduced using the edge force model [58]. According to this model, the nondiagonal stress component, i.e., shear stress component, is induced in Si at the edge of the SiN film.

The stress distribution around the edge of the stress film is validated using the following equations of the edge force model [58]:

$$\sigma_{xx} = -\frac{2F_x}{\pi} \cdot \frac{x^3}{(x^2 + z^2)^2}, \tag{33-1}$$

$$\sigma_{zz} = -\frac{2F_x}{\pi} \cdot \frac{xz^2}{(x^2 + z^2)^2}, \tag{33-2}$$

$$\tau_{xz} = -\frac{2F_x}{\pi} \cdot \frac{x^2 z}{(x^2 + z^2)^2}, \tag{33-3}$$

where σ_{xx} and σ_{zz} are the normal stress components in the direction of the x and z axes, respectively. τ_{xz} is the nondiagonal stress component (shear stress component). F_x is the tangential stress at the interface of the stress film and a substrate at the edge of the stress film, which is represented by $f \times t$, where f and t are the inner stress and the film thickness, respectively [58]. Each stress component is a function of x and z, which correspond to the lateral and depth directions of the substrate, respectively. The displacement along the y direction can be ignored because of the geometry. The plane strain assumption gives the stress components σ_{xx}, σ_{yy}, σ_{zz}, and τ_{xz}. Therefore, the stress tensor is represented by:

$$\sigma = \begin{pmatrix} \sigma_{xx} & 0 & \tau_{xz} \\ 0 & \sigma_{yy} & 0 \\ \tau_{xz} & 0 & \sigma_{zz} \end{pmatrix} \tag{34}$$

Fig. 11 shows the stress distribution in the substrate around the edge of the stress film, as calculated by Eq. 33. The inner stress of the film is assumed to be compressive (−1.0 GPa), and the film thickness is 80 nm. The positive and negative values indicate tensile and compressive stresses, respectively. First, large stress is induced around the edge of the stress film. The stress distribution around the edge is steep, especially for the stress components σ_{zz} and τ_{xz}. This fact indicates that high spatial resolution is needed to evaluate the nondiagonal stress component. Second, the opposite stress components σ_{xx} and σ_{zz} are confirmed between the region under the stress film and the space region; tensile stress appears in the region under the stress film, whereas compressive stress appears in the space region.
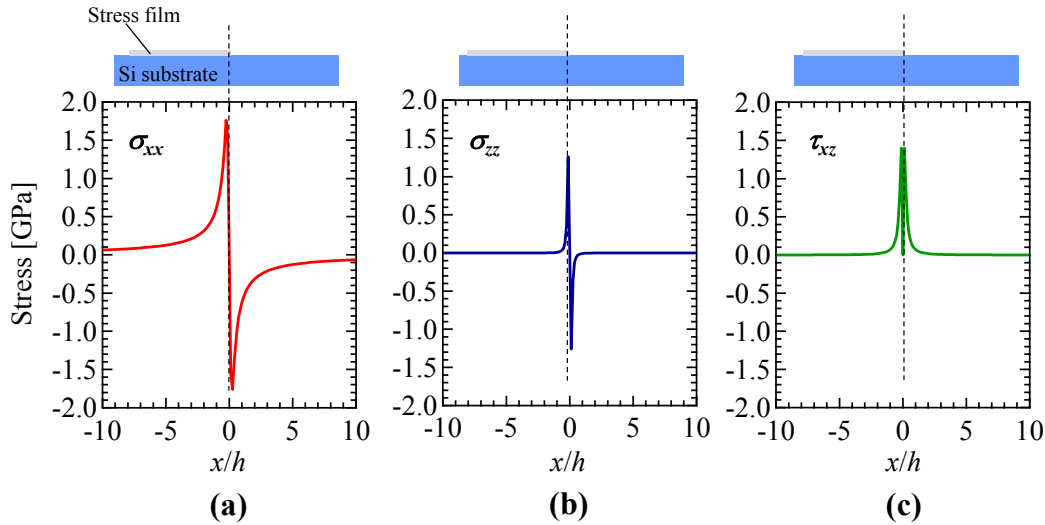

Figure 11. Stress distributions in Si calculated by (a) Eq. (33-1), (b) Eq. (33-2), and (c) Eq. (33-3).

2.5. Experimental configurations

We selectively obtained each optical phonon mode in Si by controlling incident and scattered electrical fields using polarizers and by sample rotation, which was based on the Raman polarization selection rules expressed by Eq. (1). Fig. 12 shows the various polarization configurations in liquid-immersion Raman spectroscopy. In the case of configuration (a), the LO phonon mode is Raman active. As shown in Fig. 12(a), the directions of the incident and scattered electrical fields are parallel to each other. The parallel-polarization configuration is generally applied in conventional Raman spectroscopy. On the other hand, the cross-polarization configuration by rotating the polarizer by 90° for the scattered light shown in Fig. 12(b) results in the fact that the TO phonon modes are Raman active. The TO phonon modes are excited by the z polarization due to the high-NA liquid-immersion lens. In this case, the peak separation of the two TO phonon modes is needed in the analysis. In the case of configuration (c), the sample is rotated by 45° in the parallel-polarization configuration. In this case, one of the two TO phonon modes is Raman active. In the experiments, we applied the configurations (a) and (c) to separately obtain the LO and TO phonon modes.

For the measurements of nondiagonal sress components in Si, the dependence of the Raman spectra from Si at the edge of the SiN film on the relative polarization direction between the sample orientation and the electrical fields of incident and scattered light was analyzed in detail. The experimental polarization configuration in liquid-immersion Raman spectroscopy is shown in Fig. 13. Both of the polarizations of the excitation laser and the scattered light were in the y' direction. The sample was rotated from 0° to 180°, as shown in Fig. 13.
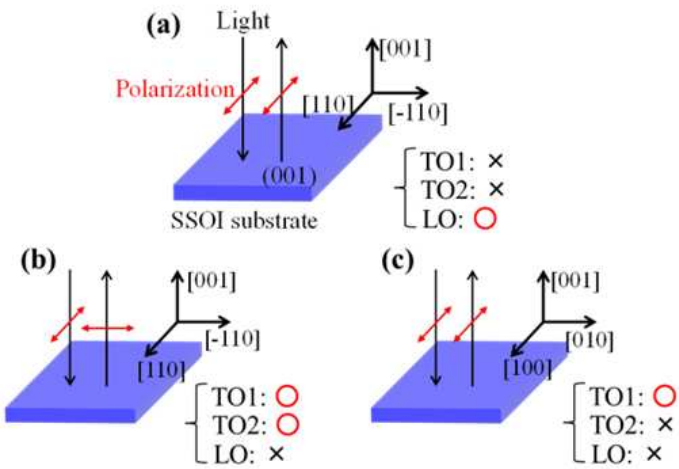
Figure 12. Polarization configurations in oil-immersion Raman spectroscopy: (a) LO active, (b) two TOs active, and (c) one of TOs active configuration
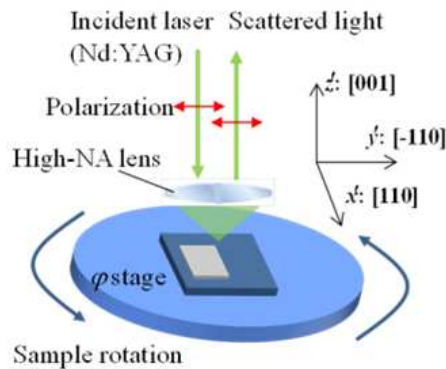
Figure 13. Polarization configuration for measurments of nondiagonal stress components in Si

Second harmonic generation of a neodymium-doped yttrium aluminum garnet (Nd:YAG) laser was used as the excitation source light in liquid-immersion Raman spectroscopy, the optical penetration depth of which is approximately 450 nm into Si [44]. The focal length of the spectroscope and the number of grating grooves were 2,000 mm and 1,800 mm^{-1}, respectively. Therefore, the high-wavenumber resolution of approximately 0.1 cm^{-1} was obtained. The detail explanations of the equipment are shown in Ref. 59. High-NA liquid-immersion lenses were used in this study. An oil-immersion lens with NA of 1.7 was used for the excitation of the TO phonon modes in the SSOI substrate with the 70-nm-thick strained Si layer. The refraction index n of the oil was 1.8. The oil-immersion lens with NA

of 1.4 (n = 1.5) was used for the measurements of the anisotropic biaxial stress states in the SSOI nanostructures and the strained SiGe nanostructures. A water-immersion lens with NA of 1.2 (n = 1.3) was used for the measurements of the nondiagonal stress components. High spatial resolution was achieved owing to the high-NA liquid-immersion lens. The beam spot size was approximately 275, 334 and 390 nm for NA of 1.7, 1.4, and 1.2 liquid-immersion lenses, respectively, according to $0.88 \times \lambda / NA$ [60]. For the oblique incident light configuration as shown in Fig. 1, NA of the objective was 0.7. The glancing angles were 30° and 90°, as shown above.

2.6. Stress calculation

Stress calculations in the SSOI nanostructures were performed by finite element method (FEM). The results of FEM were compared with the values of the anisotropic biaxial stresses σ_{xx}' and σ_{yy}' obtained by oil-immersion Raman spectroscopy. The virtual biaxial thermal expansion of Si was used and the nodes between the interface of SSOI and BOX were fixed in the FEM calculations. The initial stress value of SSOI before the etching was defined as 1.1 GPa, which was equal to the value obtained by the Raman measurements. The number of meshes was constant for all the SSOI nanostructures: the number of nodes was 13,226 and the number of elements was 11,500. The averaged stress value in the circle area with a diameter of 334 nm corresponding to the beam spot size at the center of the SSOI nanostructure was compared with the measured data. For the depth direction, the stress values throughout the SSOI thickness were averaged because the optical penetration depth of the excitation light was large enough.

3. Results and discussion

## 3.1. Excitation of TO phonon modes in oil-immersion Raman spectroscopy

Fig. 14 shows the Raman spectra of the LO phonon modes from the SSOI substrate in the oblique incident light configurations with the glancing angles of 30° and 90°. Two peaks are seen in the Raman spectra because the excitation light (λ = 532 nm) penetrates the strained Si layer, the BOX layer, and reaches the Si substrate. Therefore, the wavenumber on the high-frequency side (defined to be 520 cm^{-1} in this study) originates from the Si substrate, and the wavenumber on the low-frequency side originates from the strained Si layer with the isotropic biaxial tensile stress state. The Raman intensities obtained in the 30° and 90° configurations are almost the same, which is consistent with the calculations shown in Fig. 2. Fig. 15 shows the Raman spectrum from the SSOI substrate in the TO active configuration. The glancing angle was 30°. The fitting curves for the strained Si layer and the Si substrate are also shown in Fig. 15. The explanation about the peak positions of the LO and TO phonon modes for SSOI are shown later.

From the results, the intensity ratio of the TO phonon mode from the strained Si layer obtained in the TO active configuration to the LO phonon mode from the strained Si layer obtained in the LO active configuration was calculated to be approximately 0.04. This value

is almost the same as the theoretical value shown by Eq. (3). Using the oblique incident light configuration, the TO phonon modes were excited even for (001) Si. It is possible to completely eliminate the intensity of the LO phonon mode in the oblique incident light configuration in theory. Nevertheless, as shown in Fig. 15, the LO phonon mode was observed in the TO active configuration. This result is considered that there are misalignments of polarization between the incident/scattered light and the orientation of the Si substrate. It is considered that this behavior easily happens because the intensity of the LO phonon mode is much higher than that of the TO phonon mode.
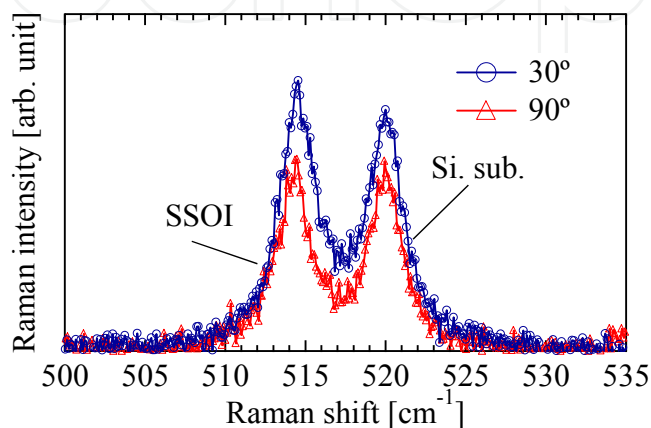
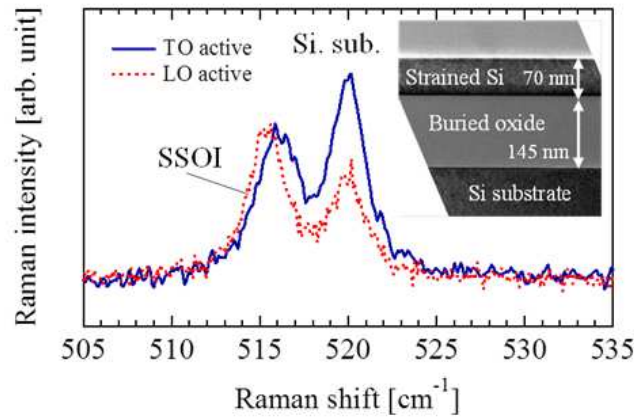**Figure 14.** Raman spectra in 30° and 90° configurations
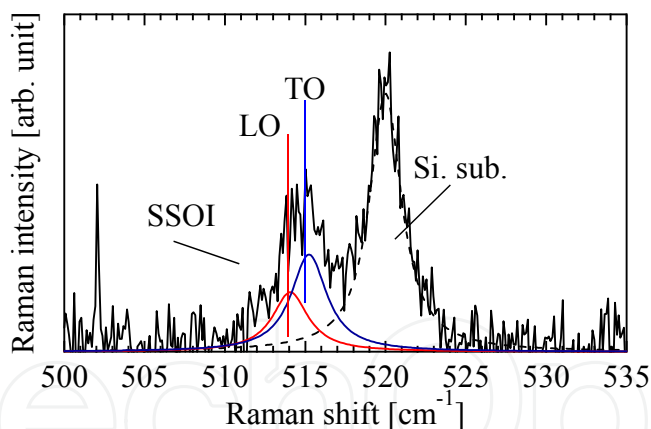
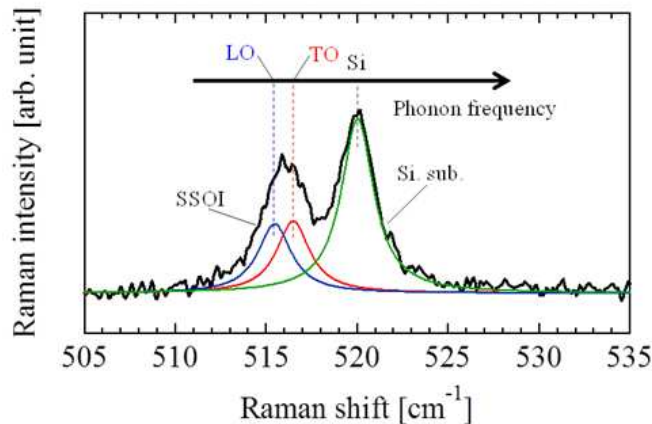**Figure 15.** Raman spectrum in TO active configuration with fitting curves

Fig. 16 shows the Raman spectra from SSOI in the LO and TO active conditions, respectively, obtained by oil-immersion Raman spectroscopy. The light-exposure time is 5 s and 300 s for the excitations of the LO and TO phonons, respectively. The Raman intensity shown in Fig. 16 was normalized by the Raman signal from the strained Si layer. It should be noted that the low-frequency peak from strained Si in the LO active condition is lower than that in the TO active condition, although the peaks from the Si substrate in each condition are at the same wavenumber. The difference of the peak positions can be explained by Eq. (17); the LO phonon mode is more affected by biaxial stress than are the TO phonon modes.

Fig. 17 shows the result of fitting each peak. The LO phonon mode is detected irrespective of the TO active condition. This fact arises because the incident light with the polarization in the [010] Si direction generates even in configuration (c) shown in Fig. 12 due to depolarization effects [24]. It is considered difficult to avoid the depolarization effects for the SSOI substrate. On the other hand, it is reported that the contribution of the LO phonon modes can be decreased for the SSOI nanostructures because the depolarization effects relax due to the nanostructure [24]. It is considered that the peak separation of the LO and TO phonon modes is needed for the SSOI substrate to analyze the Raman spectrum obtained in the TO active configuration, while not necessary for the SSOI nanostructure.

**Figure 16.** Raman spectra from SSOI in TO and LO active configurations

Figure 17. Raman spectrum in TO active configuration with fitting curves

The wavenumber shift of the LO phonon mode for the strained Si layer in the TO active configuration was −4.56 cm^{-1}, which is consistent with the value of −4.60 cm^{-1} for the Raman peak obtained in the LO active configuration. Furthermore, the Raman peak intensity from the Si substrate in the TO active condition is higher than that in the LO active configuration. This behavior indicates that the Raman peak that originates from the LO phonon mode is superimposed onto the Raman peak that originates from the TO phonon mode. We claim that the TO phonon mode was excited by using the high-NA oil-immersion lens.

Fig. 18 shows the Raman spectra from SSOI obtained by conventional Raman spectroscopy with the use of the NA = 0.7 objective. The dashed and solid lines denote the Raman spectra in the LO and TO active configurations, respectively. The light-exposure time of 3600 s for the TO active configuration is 400 times longer than that of 9 s (0.25% of 3600 s) for the LO active configuration. The intensity ratio of the TO to LO phonon modes are anticipated by the calculation shown in Table 2. In Fig. 18, the Raman intensity in each configuration is close to one another. Furthermore, the difference of the peak positions of the strained-Si layer in each configuration is confirmed, similarly to the results in oil-immersion Raman spectroscopy. These results indicate that the TO phonon mode was excited even in conventional Raman spectroscopy. However, the signal to noise ratio of the Raman intensity is bad. Moreover, the extremely long time measurements are necessary. In fact, it is difficult to perform mapping for obtaining biaxial-stress distributions in conventional Raman spectroscopy. We consider that it is important to use the high-NA liquid-immersion lens in order to excite TO phonon mode effectively and obtain biaxial-stress distributions in a realistic time.
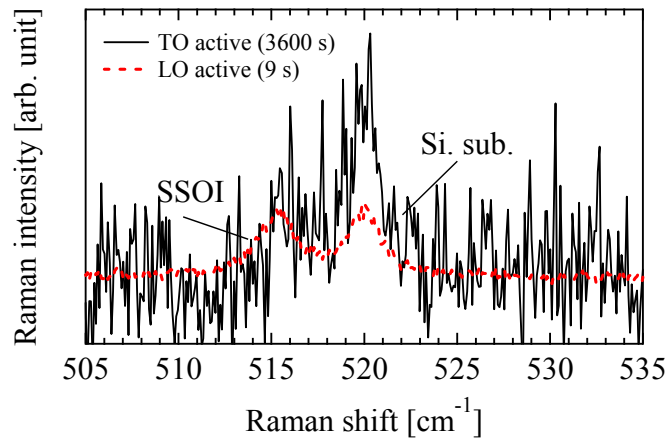
**Figure 18.** Raman spectra from SSOI with use of dry objective.

3.2. Measurements of anisotropic biaxial stress states in SSOI nanostructures

In-plane XRD measurements were performed to confirm strain in the strained Si layer. The diffraction from Si (220) and (–220) were measured (the results are not shown). As a result, ε_{xx} and ε_{yy} were 7.5×10^{-3} and 7.4×10^{-3}, respectively. These results indicate that the stress state in the strained Si layer is almost isotropic biaxial throughout the wide area which is equivalent to the footprint of the incident X-ray.

PDPs were evaluated by oil-immersion Raman spectroscopy. The calculated biaxial stresses σ_{xx} and σ_{yy} in the strained Si layer are summarized in Fig. 19. In the calculation of the biaxial stresses, PDPs reported in 1970, 1978, and 1990, as mentioned above, were used and Eqs. (19)-(21) were used for the stress calculations. In the oil-immersion Raman measurements, five points were obtained. The solid symbols indicate the average values. From the results, it appears that the biaxial stress values fluctuate in the range of 50–150 MPa, which is attributed to the dislocation conditions in the strained Si layer [61-63]. It should be noted

that the apparent anisotropic natures of biaxial stress states were observed in the case of using PDPs reported in 1970 and 1978. The differences in the biaxial stresses are 530 and 170 MPa for PDPs reported in 1970 and 1978, respectively, which are inconsistent with the results of XRD. On the other hand, the isotropic nature was clearly observed in the case of using PDPs reported in 1990. As a result, PDPs of $p/\omega^2 = -1.85$, $q/\omega^2 = -2.31$, and $r/\omega^2 = -0.71$ reported by Anastassakis et al. in 1990 are considered the most accurate for evaluating stress in Si among the three sets of PDPs.

Figs. 20(a) and (b) show the Raman spectra from the SSOI nanostructures with W = 1.0 and 0.05 μm, respectively, in configuration (c). Ls of the nanostructures were both 5.0 μm. We subtracted the signal of the Si substrate fitting curves from the raw data in order to analyze the spectra from the SSOI nanostructures in detail. From Fig. 20(b), the signal from the SSOI nanostructure even with W = 50 nm can be clearly observed. This observation is attributed to the high spatial resolution in oil-immersion Raman spectroscopy.
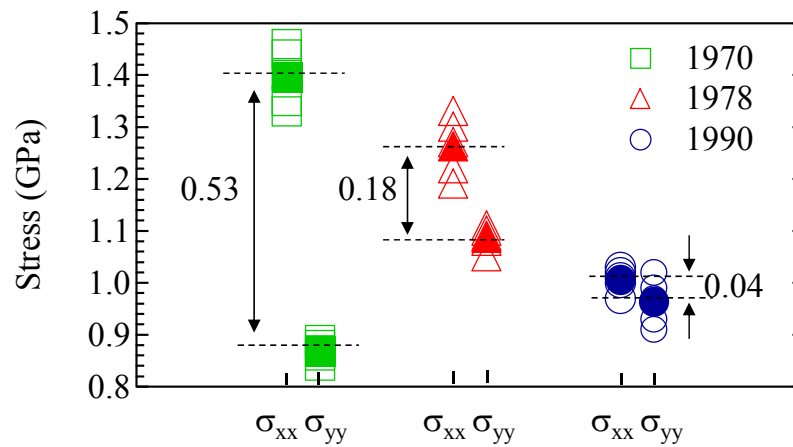

Figure 19. Biaxial stresses σ_{xx} and σ_{yy} in SSOI obtained by oil-immersion Raman spectroscopy using three sets of PDPs.
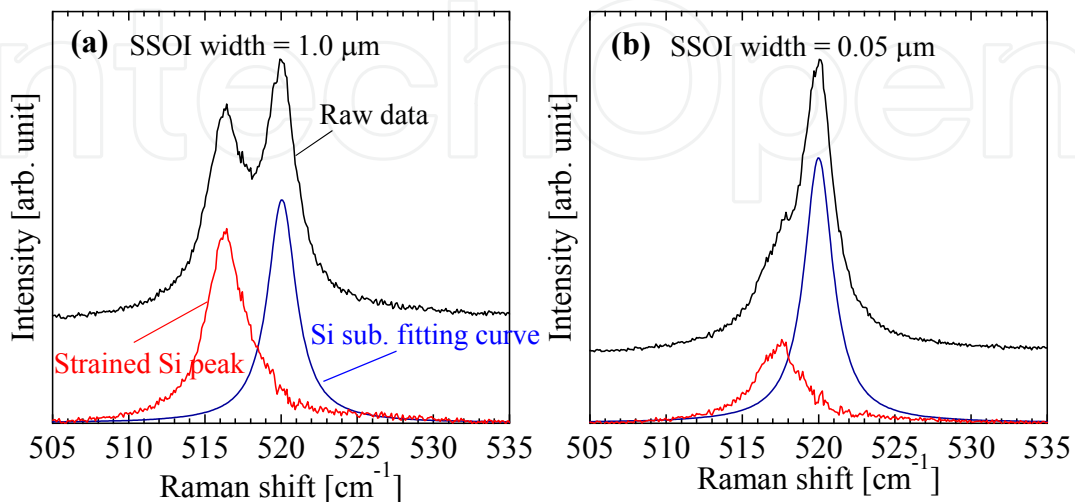
Figure 20. Rama spectra from SSOI nanostructures with Ws of (a) 1.0 and (b) 0.05 μm. L is both 5.0 μm.

The normalized Raman spectra as a function of L are shown in Fig. 21. W was fixed to 0.2 μm. The peaks from bulk Si are shown for comparison. The peak positions of strained Si gradually shift toward the high-frequency side with the decrease in L from 5.0 to 0.5 μm, as shown in Fig.21. Using Eq. (21), the anisotropic biaxial stresses σ_{xx}' and σ_{yy}' in the SSOI nanostructures were calculated, as shown in Fig. 22. Figs. 22(a) and (b) show the results for the SSOI nanostructures with the thickness of 50 and 30 nm, respectively. The results of the Raman measurements were compared with those of FEM. The example of the FEM calculations is shown in Fig. 23. Fig. 23 shows the three dimensional distribution of the σ_{xx}' component for the SSOI nanostructure with $L = 1.0$ and $W = 0.2$ μm. From the results of FEM, the stress relaxation is confirmed at the edge of the SSOI nanostructure, while large tensile stress remains in the center of the SSOI nanostructure and at the interface of the strained Si layer and the BOX layer. There is a good correlation between the results of oil-immersion Raman spectroscopy and FEM, as shown in Fig. 22. σ_{xx}' decreases with the decrease in L for the SSOI nanostructures with the thickness of 50 and 30 nm, while σ_{yy}' remains almost constant. Moreover, the values of σ_{yy}' for the SSOI nanostructures with the thickness of 30 nm are larger than those of 50 nm. Therefore, the thin SSOI nanostructures had immunity to the stress relaxation. Using oil-immersion Raman spectroscopy, the evaluation of the anisotropic biaxial stress states was accomplished for the SSOI nanostructures. It is considered that the results obtained in this study have important implications for the SSOI nanostructure fabrication.
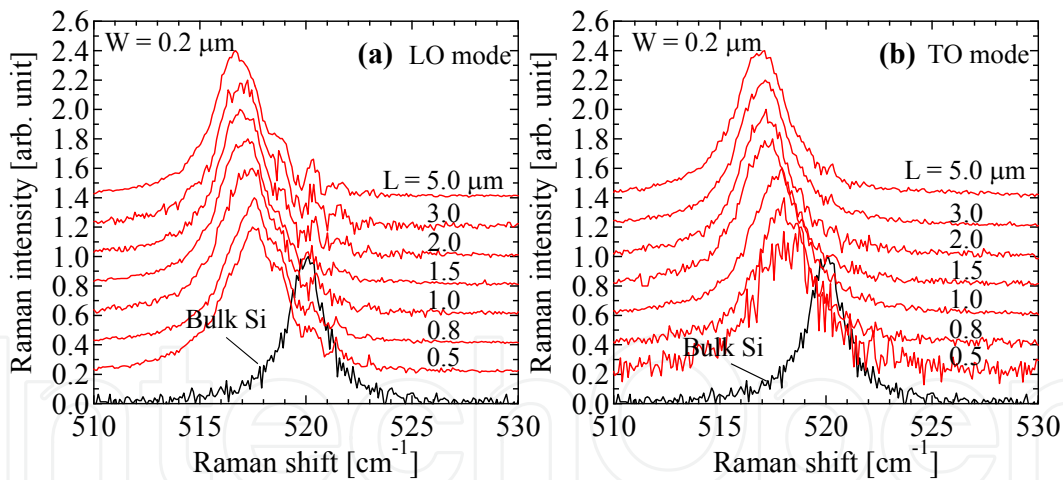

Figure 21. Normalized Raman spectra from SSOI nanostructures as a function of L in (a) LO and (b) TO active configurations.

3.3. Measurements of anisotropic biaxial stress states in strained SiGe nanostructures

In this section, the evaluation of the anisotropic biaxial stress states in the SiGe nanostructures is shown. For the SiGe nanostructures, large compressive stress is induced because the lattice constant of SiGe is larger than that of Si. The stress states in the SiGe nanostructures are considered to be expressed by Eq. (12) similar to the stress states in the

SSOI nanostructures. The crystal structure of SiGe remains diamond type, i.e., the methodology of evaluation for the anisotropic biaxial stress in Si shown above can be directly applied to strained SiGe.
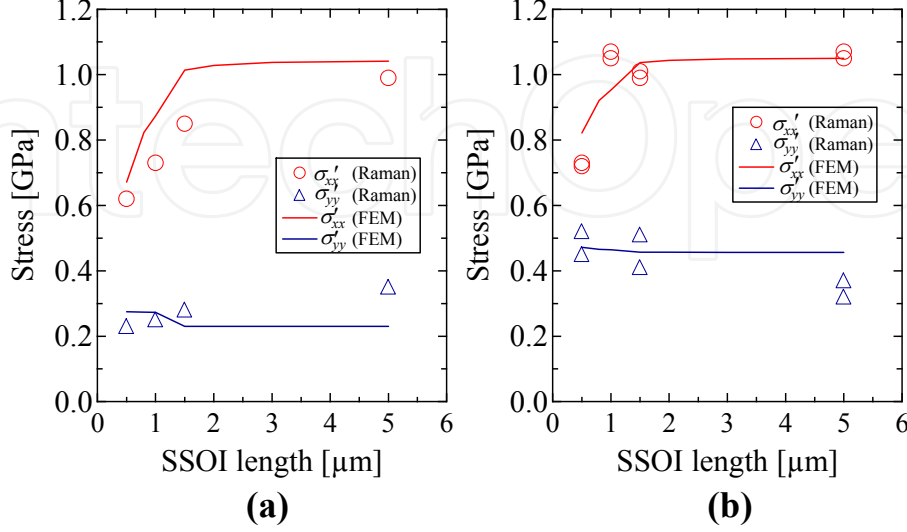

Figure 22. Biaxial stresses σ_{xx}' and σ_{yy}' as a function of L for (a) 50-nm-thick and (b) 30-nm-thick SSOI nanostructures.
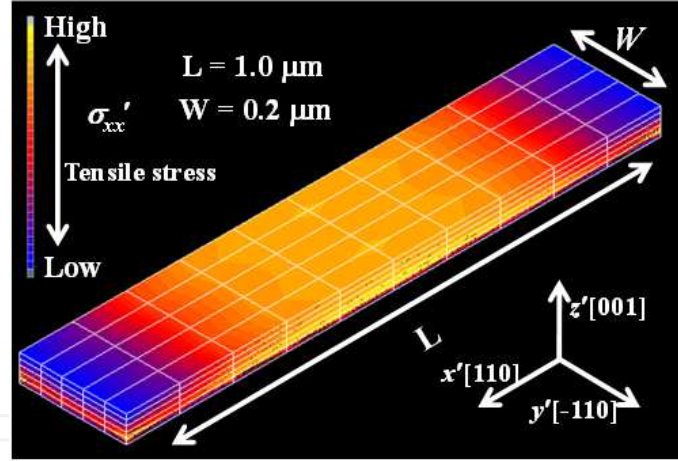
Figure 23. Three dimensional stress distribution obtained by FEM.

Fig. 24 shows the examples of Raman spectra from the SiGe nanostructures. As shown in Fig. 24, the intensity from Si-Si phonon mode in SiGe appeared to be weak, while the intensity of the Si substrate is very strong. This behavior makes the analysis difficult. Nevertheless, the LO and TO phonon modes can be separately obtained. The peak positions of the TO and LO phonon modes for the SiGe nanostructures with $L = 5.0$ and $W = 1.0$ μm are clearly different. Moreover, it should be noted that the difference decreases with the decrease in W. For $W = 0.1$ μm, there is little difference between the peak positions of the TO and LO phonon modes. This behavior indicates that the stress states in the SiGe nanostructures change from a biaxial state to a uniaxial state.
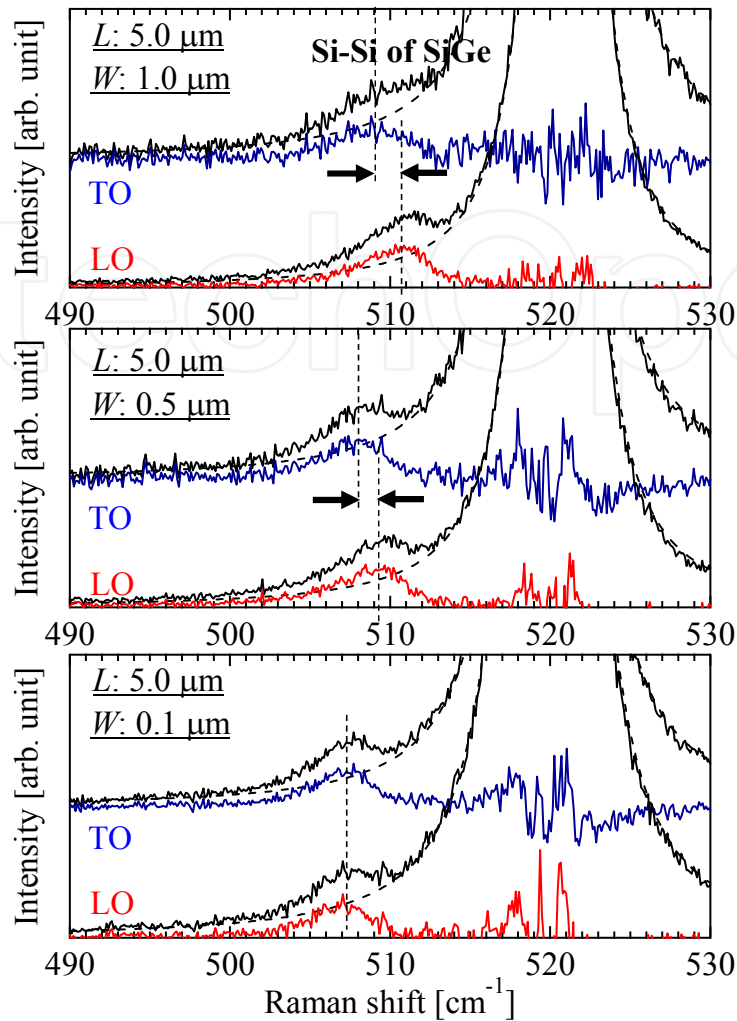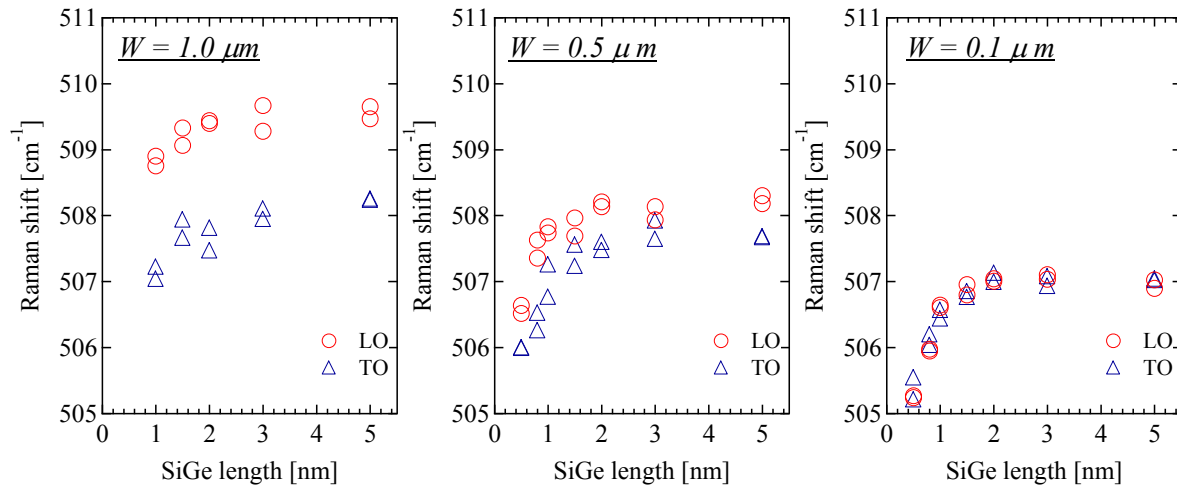
Figure 24. Raman spectra of TO and LO phonon modes from SiGe nanostructures.

Fig. 25 shows the Raman shifts of the TO and LO phonon modes for the SiGe nanostructures with W = 1.0, 0.5, and 0.1 μm as a function of L. First, the large compressive stress exists because the Raman shift of stress-free SiGe with the 30% Ge concentration is approximately 500 cm^{-1} [64,65]. From the results, the clear dependence of the Raman shifts on L and W were observed. It appears that the evaluation of the anisotropic biaxial stress states in strained SiGe is accomplished by oil-immersion Raman spectroscopy similar to evaluating strained Si. However, it is considered that the evaluation of strained SiGe is more difficult than that of Si. There are several unknown parameters for measuring stress in strained SiGe, e.g., PDPs of SiGe, precise Ge concentration, and peak position of stress-free SiGe. Various parameters have so far been suggested [64-70]. These problems are now under investigation.

3.4. Measurements of nondiagonal stress components

First, α (the contribution of z polarization) was determined from the Raman intensity ratio of the TO to LO phonon modes (the results are not shown). From the results, α was

calculated to be 0.09 in the water-immersion Raman measurements. Fig. 26 shows the comparison between the measured and calculated data of the Raman shifts dependences on the sample rotation angle. The experimental results were obtained by high-NA water-immersion Raman spectroscopy. The measurement position was the region at the edge of the SiN film (the edge under the SiN film rather than in the space region). Features indicating the induction of stress with the nondiagonal component are clearly observed in the experimental results; the profiles of the Raman shift dependence on the sample rotation angle are asymmetric relative to 45° from 0° to 90° (or relative to 135° from 90° to 180°). As previously shown, this behavior indicates that the shear stress component τ_{xz} is induced in Si at the edge of the SiN film. From Fig. 26, there is a good correlation between the measured and calculated data. On the other hand, disagreements appear around sample rotation angles of 45° and 135°. One possible explanation is that the polarization of the electrical fields of the incident and scattered light is modified by the SiN film. This modification is not included in the calculation.

Figure 25. Raman shifts of TO and LO phonon modes for SiGe nanostructures as a function of *L*.
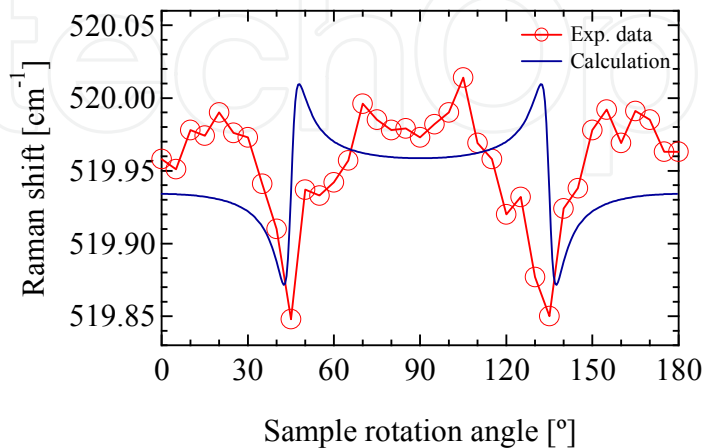
Figure 26. Comparison between measured and calculated data of Raman shift dependences on sample rotation angle.

The Raman shifts appear to be small. This is explained as follows. The stress induced at the edge of the SiN film is localized in width and depth. It is considered that the measured stress is averaged in the region of approximately 390 and 450 nm which are the spot size and optical penetration depth of the laser, respectively. From the water-immersion Raman measurements, τ_{xz}' was approximately 0.1 GPa. This value was consistent with the result obtained by the edge force model after the correction for the spot size and the optical penetration depth of the laser (the results are not shown) [46,58]. The methodology described here has the potential to measure complicated stress states in Si and SiGe even those with nondiagonal stress components.

4. Conclusion

We demonstrated the measurements of the complicated stress states in Si by high-NA liquid-immersion Raman spectroscopy. The z polarization was obtained due to the high-NA liquid-immersion lens, which allows for exciting the forbidden modes, the TO phonon modes, even under the (001) Si backscattering geometry. First, the TO phonon mode of the strained Si layer was observed in oil-immersion Raman spectroscopy. The peak positions of the strained Si layer were clearly separated in the TO and LO active configurations, although the Si substrate peaks remain at the same position in each configuration. This behavior indicates that the biaxial isotropic tensile stress state in the strained Si layer gives rise to the splitting of the optical phonon modes in Si. From the results, the LO phonon mode was more affected by biaxial stress than the TO phonon mode, which was consistent with the result obtained by solving the secular equations. Using the TO phonon mode as well as the LO phonon mode, the anisotropic biaxial stress states in the SSOI nanostructures were measured. As a result, the clear dependences of the biaxial stresses σ_{xx}' and σ_{yy}' on L and thickness were observed. σ_{xx}' decreased with the decrease in L, especially under $L = 1.5$ µm, while σ_{yy}' remains almost constant. The values of σ_{yy}' for the SSOI nanostructures with the thickness of 30 nm are larger than those of 50 nm, which indicates that the thin SSOI nanostructures had immunity to the stress relaxation. The results obtained by oil-immersion Raman spectroscopy were consistent with the FEM calculations. We also measured the anisotropic biaxial stress states in the strained SiGe nanostructures by the same technique. Consequently, the clear dependence of the Raman shifts on L and W were observed similarly to the results for the SSOI nanostructures. Furthermore, the stress with the nondiagonal component, the shear stress component, in Si was measured by water-immersion Raman spectroscopy. As a result, the asymmetric profile was obtained for the dependence of the Raman shifts on the sample rotation angle. This behavior indicates that the shear stress component τ_{xz} is induced in Si at the edge of the SiN film. There is a good correlation between the measured and calculated data. High-NA liquid-immersion Raman spectroscopy enabled us to measure the complicated stress states in strained Si and SiGe with high spatial resolution even those with the nondiagonal stress component.

Author details

Daisuke Kosemura, Motohiro Tomita and Atsushi Ogura
School of Science and Technology, Meiji University, Kawasaki, Japan

Koji Usuda
Green Nanoelectronics Collaborative Research Center, AIST, Tsukuba, Ibaraki, Japan

5. Acknowledgement

6. References

[1] S. Takagi, J. L. Hoyt, J. Welser, and J. F. Gibborns, J. Appl. Phys. 80, 1567 (1996).

[2] C. S. Smith. Phys. Rev. 94, 42 (1964).

[3] A. Ogura, D. Kosemura, K. Yamasaki, S. Tanaka, Y. Kakemura, A. Kitano, and I. Hirosawa, Solid-State Electronics 51, 219 (2007).

[4] K. Usuda, T. Irisawa, T. Numata, N. Hirashita, and S. Takagi, Semicond. Sci. Technol. 22, s227 (2007).

[5] K. Usuda, T. Mizuno, T. Tezuka, N. Sugiyama, Y. Moriyama, S. Nakaharai, S. Takagi, Appl. Surf. Sci. 224, 113 (2004).

[6] A. Ogura, T. Yoshida, D. Kosemura, Y. Kakemura, M. Takei, H. Saito, T. Shimura, T. Koganezawa, and H. Hirosawa, Solid-State Electronics 52, 1845 (2008).

[7] M. Takei, D. Kosemura, K. Nagata, H. Akamatsu, S. Mayuzumi, S. Yamakawa, H. Wakabayashi, and A. Ogura, J. Appl. Phys. 107, 124507 (2010).

[8] M. Takei, H. Hashiguchi, T. Yamaguchi, D. Kosemura, K. Nagata, and Atsushi Ogura, Jpn. J. Appl. Phys. 51, 04DA04 (2012).

[9] D. Kosemura, Y. Kakemura, T. Yoshida, A. Ogura, M. Kohno, T. Nishita, and T. Nakanishi, Jpn. J. Appl. Phys. 47, 2538 (2008).

[10] A. Ogura, H. Saitoh, D. Kosemura, Y. Kakemura, T. Yoshida, M. Takei, T. Koganezawa, I. Hirosawa, M. Kohno, T. Nishita, and T. Nakanishi, Electrochem. Solid-State Lett. 12, H117 (2009).

[11] S. Mayuzumi, S. Yamakawa, D. Kosemura, M. Takei, Y. Tateshita, H. Wakabayashi, M. Tsukamoto, T. Ono, A. Ogura, and N. Nagashima, IEEE Transactions on Electron Devices 56, 2778 (2009).

276 Advanced Aspects of Spectroscopy

[12] T. Yamaguchi, Y. Kawasaki, T. Yamashita, N. Miura, M. Mizuo, J. Tsuchimoto, K. Eikyu, K. Maekawa, M. Fujisawa, and K. Asai, Jpn. J. Appl. Phys. 50, 04DA02 (2011).

[13] W. Xiong, C. R. Cleavelin, P. Kohli, C. Huffman, T. Schulz, K. Schruefer, G. Gebara, K. Mathews, P. Patruno, Y.-M. L. Vaillant, I. Cayrefourcq, M. Kennard, C. Mazure, K. Shin, and T.-J. K. Liu, IEEE Electron Device Lett. 27, 612 (2006).

[14] M. Tomita, D. Kosemura, M. Takei, K. Nagata, H. Akamatsu, and A. Ogura, Jpn. J. Appl. Phys. 50, 010111 (2011).

[15] M. D. Vaudin, Y. B. Gerbig, S. J. Stranick, and R. F. Cook, Appl. Phys. Lett. 93, 193116 (2008).

[16] K. Omote, J. Phys., Condens. Matter. 22, 474004 (2010).

[17] I. D. Wolf, Semicond. Sci. Technol. 11, 139 (1996).

[18] L. Zhu, C. Georgi, M. Hecker, J. Rinderknecht, A. Mai, Y. Ritz, and E. Zschech, J. Appl. Phys. 101, 104305 (2007).

[19] S. C. Jain, B. Dietrich, H. Richter, A. Atkinson, and A. H. Harker, Phys. Rev. B 52, 6247 (1995).

[20] T. Ito, H. Azuma, and S. Noda, Jpn. J. Appl. Phys. 33, 171 (1994).

[21] S. Nakashima, T. Mitani, M. Ninomiya, and K. Matsumoto, J. Appl. Phys. 99, 053512 (2006).

[22] D. Kosemura and A. Ogura, Appl. Phys. Lett. 96, 212106 (2010).

[23] V. Poborchii, T. Tada, and T. Kanayama, Appl. Phys. Lett. 97, 041915 (2010).

[24] A. Tarun, N. Hayazawa, H. Ishitobi, S. Kawata, M. Reiche, and O. Moutanabbir, Nano Lett. 11, 4780 (2011).

[25] E. Bonera, M. Fanciulli, and D. N. Batchelder, J. Appl. Phys. 94, 2729 (2003).

[26] S. Narayanan, S. R. Kalidindi, and L. S. Schadler, J. Appl. Phys. 82, 2595 (1997).

[27] M. Yoshikawa, M. Maegawa, G. Katagiri, and H. Ishida, J. Appl. Phys. 78, 941 (1995) 941.

[28] M. Becker and H. Scheel, J. Appl. Phys. 101, 063531 (2007).

[29] S. J. Harris, A. E. O'Neill, W. Yang, P. Gustafson, J. Boileau, W. H. Weber, B. Majumdar, and S. Ghosh, J. Appl. Phys. 96, 7195 (2004).

[30] D. Kosemura and A. Ogura, Jpn. J. Appl. Phys. 50, 04DA06 (2011).

[31] D. Kosemura, M. Tomita, K. Usuda, and A. Ogura, Jpn. J. Appl. Phys. 51, 02BA03 (2012).

[32] V. Poborchii, T. Tada, K. Usuda, and T. Kanayama, Appl. Phys. Lett. 99, 191911 (2011).

[33] R. Ossikovski, Q. Nguyen, G. Picardi, and J. Schreiber, J. Appl. Phys. 103, 093525 (2008).

[34] T. Tada, V. Poporchii, and T. Kanayama, J. Appl. Phys. 107, 113539 (2010).

[35] G. H. Loechelt, H. G. Cave, and J. Menendez, J. Appl. Phys. 86, 6164 (1999).

[36] P. Kumar, I. Dutta, and M. S. Bakir, J. Electronic Mater. 41, 322 (2011).

[37] M. Feron, Z. Zhang, and Z. Suo, J. Appl. Phys. 102, 023502 (2007).

[38] Y. Moriyama, Y. Kamimuta, Keiji Ikeda, Tsutomu Tezuka, Thin Solid Films 520, 3236 (2012).

[39] K. Ikeda, M. Oda, Y. Kamimuta, Y. Moriyama, and T. Tezuka, Appl. Phys. Exp. 3, 124201 (2010).

[40] T. Tezuka, E. Toyoda, T. Irisawa, N. Hirashita, Y. Moriyama, N. Sugiyama, K.Usuda, and S. Takagi, Appl. Phys. Lett. 94, 081910 (2009).

[41] T. Irisawa, T. Numata, T. Tezuka, K. Usuda, N. Hirashita, N. Sugiyama, E. Toyoda, and S. Takagi, IEEE Transactions on Electron Devices 53, 2809 (2006).

[42] E. Anastassakis, J. Appl. Phys. 82, 1582 (1997).

[43] R. Loudon, Adv. Phys. 13, 423 (1964).

[44] D. E. Aspnes and A. Studna, Phys. Rev. B. 27, 985 (1983).

[45] K. Mizoguchi and S. Nakashima, J. Appl. Phys. 65, 2583 (1989).

[46] I. D. Wolf, H. E. Maes, and S .K. Jones, J. Appl. Phys. 79, 7148 (1996).

[47] L. H. Wong, C. C. Wong, J. P. Liu, D. K. Sohn, L. Chan, L. C. Hsia, H. Zang, Z. H. Ni, and Z. X. Shen, Jpn. J. Appl. Phys. 44, 7922 (2005).

[48] Ogura A *et al* 2007 Report of JEITA Standard Strain MeasurementWorking Group JEITA.

[49] E. Anastassakis, A. Pinczuk, E. Burstein, F. H. Pollak, and M. Cardona, Solid State Commun. 8, 133 (1970).

[50] M. Chandrasekhar, J. B. Renucci, and M. Cardona, Phys. Rev. B 17, 1523 (1978).

[51] E. Anastassakis, A. Cantarero, and M. Cardona, Phys. Rev. B 41, 7529 (1990).

[52] E. Anastassakis, J. Appl. Phys. 81, 3046 (1997).

[53] O. Moutanabbir, M. Reiche, A. Ha¨hnel, M. Oehme, and E. Kasper, Appl. Phys. Lett. 97, 053105 (2010).

[54] T. S. Drake, C. Ni Chleirigh, M. L. Lee, A. J. Pitera, E. A. Fitzgerald, D. H. Anjum, J. Li, R. Hull, N. Klymko, and J. L. Hoyt, Appl. Phys. Lett. 83, 875 (2003).

[55] A. Ogura and O. Okabayashi, Thin Solid Films 488, 189 (2005).

[56] A. Ogura, T. Tatsumi, T. Hamajima, and H. Kikuchi, Appl. Phys. Lett. 69, 1367 (1996).

[57] M. Finot, I. A, Blech, S. Suresh, and H. Fujimoto, J. Appl. Phys. 81, 3457 (1997).

[58] S. M. Hu, J. Appl. Phys. 50, 4661 (1979).

[59] A. Ogura, K. Yamasaki, D. Kosemura, S. Tanaka, I, Chiba, and R. Shimidzu, Jpn. J. Appl. Phys. 45, 3007 (2006).

[60] I. D. Wolf, Theoretical and experimental study of the effects of the different optical parameters and lenses on the spatial resolution of the Raman system, STREAM consortium, Doc. No. IST-1999-10341, pp. 1-20.

[61] S. Nakashima, T. Yamamoto, A. Ogura, K. Uejima, and T. Yamamoto, Appl. Phys. Lett. 84, 2533 (2004).

[62] K. Kutsukake, N. Usami, T. Ujihara, K. Fujiwara, G. Sazaki, and K. Nakajima; Appl. Phys. Lett. 85, 1335 (2004).

[63] K. Sawano, S. Koh, Y. Shiraki, N. Usami, and K. Nakagawa, Appl. Phys. Lett. 83, 4339 (2003).

[64] J. C. Tsang, P. M. Mooney, F. Dacol, and J. O. Chu, J. Appl. Phys. 75, 8098 (1994).

[65] M. I. Alonso and K. Winer, Phys. Rev. B 39, 10056 (1989).

[66] D. J. Lockwood and J.-M. Baribeau, Phys. Rev. B 45, 8565 (1992).

[67] M. Holtz, W. M. Duncan, S. Zollner, and R. Liu, J. Appl. Phys. 88, 2523 (2000).

[68] F. Pezzoli, E. Bonera, E. Grilli, M. Guzzi, S. Sanguinetti, D. Chrastina, G. Isella, H. von Känel, E. Wintersberger, J. Stangl, and G. Bauer, J. Appl. Phys. 103, 093521 (2008).

[69] J. P. Dismukes, L. Ekstrom, and R. J. Paff, J. Phys. Chem. 68, 3021 (1964).

[70] F. Cerdeira, A. Pinczuk, J. C. Bean, B. Batlogg, and B. A. Wilson, Appl. Phys. Lett. 45, 1138 (1984).

[71] Y. Hoshi, A. Fukumoto, K. Sawano, I. Cayrefourcq, M. Yoshimi, and Y. Shiraki, Jpn. J. Appl. Phys. 46, 7294 (2007).